Proceedings of the The 27th International Conference on Electrical Machines and Systems (ICEMS), Fukuoka, Japan, November, 2024

“Current Source Inverter Drive System with Equivalent DC-Machine Control Characteristics”

S. Mirić,
P. Pejović,
T. Ohno,
M. Haider,

The 27th International Conference on Electrical Machines and Systems
(ICEMS2024-Fukuoka)

Current Source Inverter Drive System with Equivalent DC-Machine Control Characteristics

Spasoje Mirić[1], Predrag Pejović[2] Takanobu Ohno[1], and Michael Haider
[1] Drives and Energy Systems Laboratory, University of Innsbruck, 6020 Innsbruck, Austria
[2] School of Electrical Engineering, University of Belgrade, 11120 Belgrade, Serbia
Email: spasoje.miric@uibk.ac.at

***Abstract*—Current source inverters (CSIs) present several advantages over voltage source inverters (VSIs) in drive system applications, particularly when supplying motor windings. CSIs inherently feature integrated output capacitors that deliver smooth voltages to the motor windings, effectively eliminating issues such as interturn overvoltages, insulation degradation due to large d*v*/d*t*, bearing currents, and electromagnetic interference. With the recent advancements in monolithic bidirectional switches, CSIs have become an increasingly attractive option for drive systems. However, CSIs are more complex to modulate and control compared to VSIs, which poses a challenge to their widespread adoption in the industry, where engineers are typically more familiar with VSI PWM techniques. To address this, we propose the *Equivalent DC Machine* (E-DCM) concept. In this concept, the CSI operates in open loop with a fixed modulation index, relieving the user of any need to manage the CSI. The user can directly control the PMSM torque through the DC link current. As a result, the E-DCM concept enables the CSI-supplied PMSM to behave like a traditional DC machine, offering the simplicity of control without the issues associated with commutation and maintenance. To validate the proposed E-DCM concept, we provide transient time-domain simulations demonstrating its performance as it accelerates from zero to nominal speed.**

***Index Terms*—AC Machine, DC Machine, Drive Systems, Current Source Inverter, CSI, PMSM**

I. Introduction

In three-phase variable speed drive systems, voltage source inverters (VSIs) are commonly used to supply motors. Typically, VSIs directly connect to the motor windings, meaning the motor winding is wired to the switching node of the VSI bridge leg. Due to this direct connection, the motor windings are exposed to square-wave voltages, which can lead to several issues, including interturn overvoltages that can reach up to twice the DC link voltage [1], harmonic losses caused by high-frequency components in the stator current [2], bearing currents [3], electromagnetic interference (EMI) [4], and insulation aging due to high $\mathrm{d}v/\mathrm{d}t$ [5]. These challenges have become even more pronounced with the transition from IGBTs to wide bandgap (WBG) devices, due to the significantly higher switching speeds. To address these issues in VSIs, solutions like $\mathrm{d}v/\mathrm{d}t$ filters [6], or full sine wave filters have been proposed [7], [8]. However, these solutions increase the size and complexity of VSIs, thereby diminishing some of the advantages of WBGs in drive system applications.

In contrast to VSIs, current source inverters (CSIs) inherently provide smooth voltages at the motor terminals due to the output capacitors, which are integral to the CSI design. These smooth voltages eliminate typical issues in VSIs associated with high-frequency switching and pulsed voltage. For example, due to smooth voltages at the motor windings, there are no interturn overvoltages. Therefore, CSIs allow for thinner interturn insulation, which improves the slot fill factor and, consequently, the machine's power density [9]. Moreover, the boost capability of CSIs makes them well-suited for wide voltage ranges, supporting wide speed operation of motors, and positioning them as an excellent choice for high-speed machines [10]. Additionally, CSIs are strong candidates for motor-inverter integration, as they feature a DC-link inductor instead of a DC-link capacitor that is typically electrolytic or film type in VSIs, making them more robust and capable of withstanding higher temperatures [11]. In this high-temperature aspect, it should be noted that CSI output capacitors have a lower capacitance value compared to the DC link capacitors in VSIs and can be implemented using ceramic capacitors, which are well-suited for high-temperature applications.

One disadvantage of CSIs compared to VSIs is that they require switches capable of blocking voltage and current in both directions. Traditionally, this can be achieved by connecting a MOSFET and a diode in anti-series for two-quadrant operation or by connecting two MOSFETs in anti-series for four-quadrant operation. As a result, a three-phase CSI with a four-quadrant operation requires a total of 12 MOSFETs. This complexity has historically made three-phase CSIs less commonly used in industry compared to three-phase VSIs, which only require 6 MOSFETs. However, recent advancements in semiconductor technology have introduced the monolithic bidirectional switch (MBDS), based on GaN technology [12], which can block voltage and current in both directions. This allows a three-phase CSI to be realized with just 6 MBDSs. These advancements have renewed interest in CSIs for industrial applications, which is quite beneficial as CSIs can effectively address many high-frequency issues present in VSIs.

Another disadvantage of CSIs compared to VSIs is that CSIs require an input converter to regulate the DC link current, such as a CSI rectifier supplied by the power grid [13], or an input buck converter when supplied by a DC voltage source [10]. However, in certain applications, a VSI system also requires an additional input converter.

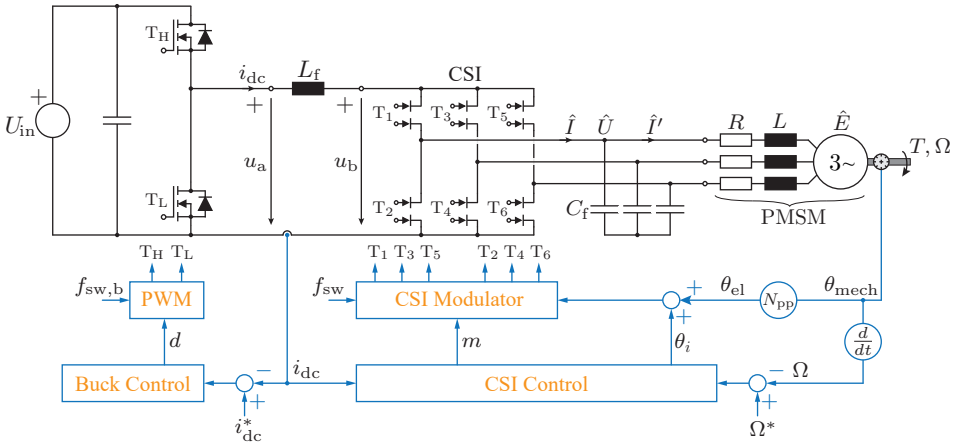

Fig. 1: Typical CSI variable speed drive system with PMSM, where U_{in} represents the supply voltage, such as a fuel cell with significant voltage variation [10]. The input buck converter regulates the DC link current through L_{f}, while the output capacitors C_{f} filter the high-frequency current components, ensuring smooth voltage supply to the PMSM windings.

For instance, in fuel cell applications, due to large voltage variations, a VSI needs an input boost converter to adjust the DC link voltage [10]. In this case, the input converter is not a disadvantage for a CSI as the bridge leg used for the boost converter can be repurposed as a buck leg to control the DC link current for the CSI, as shown in **Fig. 1**, resulting in similar realization effort for VSI and CSI. It is worth noting that some CSI drive systems attempt to bypass the need for an input converter by directly controlling the DC link current through the CSI itself. However, this approach requires an additional leg to perform short-circuit operations [14].

The CSI-based variable speed drive system shown in **Fig. 1** consists of two stages: the input buck converter, which uses the input voltage U_{in} to regulate the DC link current i_{dc}, and the CSI, which modulates the DC link current to achieve the desired output current reference. As illustrated in **Fig. 1**, the control of the stages is typically coupled. A reference for the DC link current is provided externally for the *Buck Control* block, and its measured value also has to be fed back to the *CSI Control* block, which requires it to determine the appropriate modulation index m for achieving the desired output AC currents. The *CSI Control* manages the speed control, typically with a PI speed controller that generates a torque reference, from which the modulation index m is calculated. The current angle θ_i is usually fixed at $\frac{\pi}{2}$, but can be adjusted if field weakening of the PMSM is required.

One challenge hindering the widespread adoption of such CSI drive systems in the industry is their complex control structure, which involves coupling between the two stages. Moreover, engineers are far more familiar with controlling and modulating VSIs, which are widely used, compared to CSIs, which have been less popular due to the lack of suitable switches (such as the now available MBDS). Therefore, to simplify the control of the CSI drive system (see **Fig. 1**) and decouple the connection between the buck converter and the CSI, this paper proposes an open-loop control for the CSI. In this approach, the CSI modulation index is fixed at a constant value $m = M$, and the current angle is set to a constant value $\theta_i = \theta_I$. The key advantage of this system is that the user does not need to manage the CSI control, as in this case torque control can be achieved directly by regulating the DC link current, i.e., with m and θ_i values fixed, the PMSM torque T becomes directly proportional to the DC link current i_{dc}. Ultimately, this approach makes CSI-supplied PMSM behave like a DC machine. To further simplify practical implementations, a dedicated IC (based on this approach) can be designed to handle CSI open-loop control and modulation, making the use of CSI drive systems exceptionally straightforward for the users.

To better understand the proposed open-loop operation of the CSI, we derive the DC side equivalent circuit of the CSI in **Sec. II**. This is particularly important because, with the input buck converter, we now directly control the PMSM torque. In **Sec. III**, we demonstrate that the open-loop operated CSI behaves like a DC machine from the DC side. Therefore, we refer to this control concept as the *Equivalent DC Machine* (E-DCM) concept. In **Sec. IV**, we discuss the DC-side torque constant for the E-DCM control concept. **Sec. V** presents simulation results that fully validate the E-DCM concept, and **Sec. VI** concludes the paper.

II. DC-Side Equivalent Circuit of CSI

To derive the DC-side equivalent circuit of a CSI, we consider the schematic shown in **Fig. 2**, where a DC link current is impressed on the DC side, resulting in the voltage u_{b} at the input of the CSI. It is important to note that u_{b} is pulsed voltage in reality, but our DC-side equivalent circuit will model its average value $\overline{u}_{\text{b}}$, which can be used for tasks such as controller design.

On the output side of the CSI, we assume a PMSM connected with typical parameters, including winding resistance R, phase inductance L, and back EMF voltages e_1, e_2, and e_3. With the advent of new MBDS technology, CSIs can now be built to support high switching frequencies. This allows for the use of low-capacitance

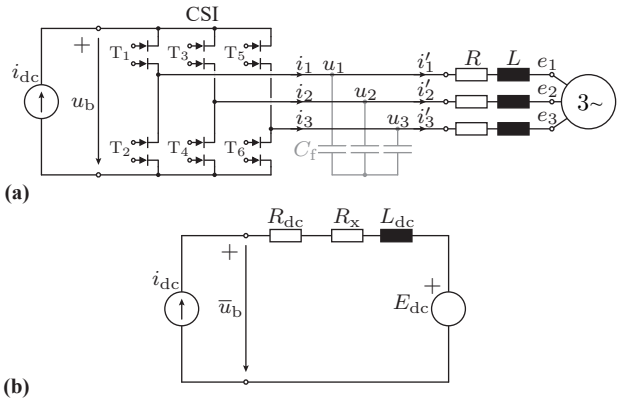

Fig. 2: (a) Circuit schematic that is used for derivation of the DC-side equivalent circuit of a CSI with a symmetrical three-phase load. Capacitors are shown in gray as their impact is neglected. **(b)** Resulting DC side equivalent circuit considering a switching frequency averaged model, i.e., $\overline{u}_\mathrm{b}$ being the local average of u_b.

output capacitors C_f, which has the advantage of minimizing the capacitor current component at the fundamental frequency. As a result, we can neglect capacitors in our analysis as it covers only the fundamental frequency range, resulting in the justified approximation $i_1 \approx i'_1$, $i_2 \approx i'_2$, and $i_3 \approx i'_3$.

The impressed DC link current i_dc, combined with the modulation index of the CSI m, determines the peak of the output current as $\hat{I} = m\, i_\mathrm{dc}$. Depending on the current angle θ_i, the instantaneous values can be obtained as

$$\begin{aligned} i_1 &= m\, i_\mathrm{dc} \cos(\theta_\mathrm{el} + \theta_i) \\ i_2 &= m\, i_\mathrm{dc} \cos(\theta_\mathrm{el} + \theta_i - \frac{2\pi}{3}), \\ i_3 &= m\, i_\mathrm{dc} \cos(\theta_\mathrm{el} + \theta_i + \frac{2\pi}{3}) \end{aligned} \tag{1}$$

where θ_el is the electrical flux angle, and θ_i is the current angle, i.e., a phase shift of the current with respect to the flux linkage of the PMSM, see **Fig. 1**. As mentioned, we neglect the C_f currents, which leads to the following voltage equations for the AC side:

$$\begin{aligned} u_1 &= R\, i_1 + L\, \frac{\mathrm{d}i_1}{\mathrm{d}t} + e_1 \\ u_2 &= R\, i_2 + L\, \frac{\mathrm{d}i_2}{\mathrm{d}t} + e_2, \\ u_3 &= R\, i_3 + L\, \frac{\mathrm{d}i_3}{\mathrm{d}t} + e_3 \end{aligned} \tag{2}$$

where the PMSM back EMFs are the time derivatives of the flux linkages, i.e., $e_1 = \frac{\mathrm{d}\psi_1}{\mathrm{d}t}$, $e_2 = \frac{\mathrm{d}\psi_2}{\mathrm{d}t}$, and $e_3 = \frac{\mathrm{d}\psi_3}{\mathrm{d}t}$. The flux linkages are equal to

$$\begin{aligned} \psi_1 &= \hat{\Psi} \cos(\theta_\mathrm{el}) \\ \psi_2 &= \hat{\Psi} \cos(\theta_\mathrm{el} - \frac{2\pi}{3}), \\ \psi_3 &= \hat{\Psi} \cos(\theta_\mathrm{el} + \frac{2\pi}{3}) \end{aligned} \tag{3}$$

where $\hat{\Psi}$ is the flux linkage of the PMSM, a critical parameter as it directly determines both the torque and voltage constants of the machine. Performing the time derivatives of the flux linkages in (3), we get the expressions for the back EMFs that are equal to

$$\begin{aligned} e_1 &= \omega \hat{\Psi} \cos(\theta_\mathrm{el} + \frac{\pi}{2}) \\ e_2 &= \omega \hat{\Psi} \cos(\theta_\mathrm{el} + \frac{\pi}{2} - \frac{2\pi}{3}), \\ e_3 &= \omega \hat{\Psi} \cos(\theta_\mathrm{el} + \frac{\pi}{2} + \frac{2\pi}{3}) \end{aligned} \tag{4}$$

where $\omega = \frac{\mathrm{d}\theta_\mathrm{el}}{\mathrm{d}t}$ is the electrical angular frequency, which can be a function of time, i.e., $\omega = \omega(t)$. Often, we will use the peak value of the back EMF in our analysis, denoted as $\hat{E}$, which is equal to

$$\hat{E} = \omega\, \hat{\Psi}. \tag{5}$$

At this stage, all necessary parameters have been defined to derive the averaged DC-side equivalent circuit of a three-phase CSI. The derivation is based on the power balance between the DC side and the three-phase AC side, which is guaranteed by the following equation

$$\overline{u}_\mathrm{b} i_\mathrm{dc} = u_1 i_1 + u_2 i_2 + u_3 i_3, \tag{6}$$

where the AC currents and voltages are given in (1) and (2), and we assume lossless CSI, see **Fig. 2(a)**. The DC-side equivalent circuit of a CSI that we will derive in the following is depicted in **Fig. 2(b)**.

A. DC-Side Equivalent Resistance

Using the equation for power balance (6), and taking only the voltage drop over the resistance R in (2), we get

$$\overline{u}_\mathrm{b}\, i_\mathrm{dc} = R\, (i_1^2 + i_2^2 + i_3^2), \tag{7}$$

where by using the expressions for the AC currents (1), we get the following

$$\overline{u}_\mathrm{b}\, i_\mathrm{dc} = \frac{3}{2} R\, m^2\, i_\mathrm{dc}^2. \tag{8}$$

If divide both sides of (8) by i_dc, we get the following voltage balance equation for the DC side

$$\overline{u}_\mathrm{b} = \underbrace{\frac{3}{2}\, m^2\, R}_{=R_\mathrm{dc}}\, i_\mathrm{dc}, \tag{9}$$

where it is easy to recognize that the DC-side equivalent resistance R_dc of the AC-side resistance R is equal to $R_\mathrm{dc} = \frac{3}{2} m^2 R$.

B. DC-Side Equivalent Inductance

Using (6) and taking only the voltage drop over the inductance L in (2), we get the following power balance for the inductance

$$\overline{u}_\mathrm{b}\, i_\mathrm{dc} = L \left(\frac{\mathrm{d}i_1}{\mathrm{d}t}\, i_1 + \frac{\mathrm{d}i_2}{\mathrm{d}t}\, i_2 + \frac{\mathrm{d}i_3}{\mathrm{d}t}\, i_3 \right). \tag{10}$$

Knowing that for any time function $f(t)$, it holds $\frac{\mathrm{d}f(t)^2}{\mathrm{d}t} = 2\, f(t) \frac{\mathrm{d}f(t)}{\mathrm{d}t}$, we can reshape (10) into the following form

$$\overline{u}_\mathrm{b}\, i_\mathrm{dc} = L\, \frac{1}{2} \left(\frac{\mathrm{d}i_1^2}{\mathrm{d}t} + \frac{\mathrm{d}i_2^2}{\mathrm{d}t} + \frac{\mathrm{d}i_3^2}{\mathrm{d}t} \right). \tag{11}$$

In (11), we can take out the time derivative in front of the brackets, resulting in the following power balance expression:

$$\overline{u}_{\mathrm{b}}\, i_{\mathrm{dc}} = L\,\frac{1}{2}\,\frac{\mathrm{d}}{\mathrm{d}t}\left(i_1^2 + i_2^2 + i_3^2\right). \tag{12}$$

Using the expression for the AC currents (1), the power balance (12) can be transformed into

$$\overline{u}_{\mathrm{b}}\, i_{\mathrm{dc}} = \frac{3}{2}\,L\,\frac{1}{2}\,\frac{\mathrm{d}(m^2\, i_{\mathrm{dc}}^2)}{\mathrm{d}t}. \tag{13}$$

After expanding the derivative of the product $(m^2\, i_{\mathrm{dc}}^2)$ in (13) and dividing both sides with i_{dc}, finally, we get the voltage balance from which we can deduce the DC-side equivalent parameters of an AC-side inductance L

$$\overline{u}_{\mathrm{b}} = \underbrace{\frac{3}{2}\,L\,m\frac{\mathrm{d}m}{\mathrm{d}t}}_{=R_{\mathrm{x}}}\, i_{\mathrm{dc}} + \underbrace{\frac{3}{2}\,m^2\,L}_{=L_{\mathrm{dc}}}\,\frac{\mathrm{d}i_{\mathrm{dc}}}{\mathrm{d}t}. \tag{14}$$

Therefore, the AC-side inductance L is seen on the DC side as a series connection of the resistance R_{x} and the inductance L_{dc}. Interestingly, in the DC-side equivalent circuit, a resistance R_{x} appears. This resistance models the power required to increase or decrease the energy in the AC-side inductance L. Therefore, it exists only when the modulation index m is changing $(R_{\mathrm{x}} \sim \frac{\mathrm{d}m}{\mathrm{d}t})$ and it can take negative values when the modulation index m decreases.

C. DC-Side Equivalent Back EMF

By taking only the back-EMF voltage component in (2) and applying it to (6), we get the power balance for back-EMF voltages

$$\overline{u}_{\mathrm{b}}\, i_{\mathrm{dc}} = e_1 i_1 + e_2 i_2 + e_3 i_3, \tag{15}$$

which we can further expand by using the expressions for the back-EMF voltages (4) and (5), resulting in

$$\overline{u}_{\mathrm{b}}\, i_{\mathrm{dc}} = \underbrace{\frac{3}{2}\, m\, \sin\theta_i\, \hat{E}}_{=E_{\mathrm{dc}}}\, i_{\mathrm{dc}} \tag{16}$$

where $E_{\mathrm{dc}} = \frac{3}{2}\, m\, \sin\theta_i\, \hat{E}$ is the DC-side equivalent back EMF. Here should be noted that the current angle θ_i suits the traditionally used dq current angle, where for the typical maximum torque per ampere, q current component $i_{\mathrm{q}} = \hat{I}\sin\theta_i$ is applied, which is equivalent to applying $\theta_i = \frac{\pi}{2}$ in the analyzed CSI, see (1) and (3).

D. Summary of the DC-Side Equivalent Circuit

The derived DC-side equivalent circuit is depicted in **Fig. 2(b)**. The expressions for the calculations of the elements are outlined in **Fig. 3(a)**. The complete DC-side circuit including the DC link inductor L_{f} is depicted in **Fig. 3(b)**. From this circuit, we can write the DC side voltage balance equation

$$\overline{u}_{\mathrm{a}} = (R_{\mathrm{dc}} + R_{\mathrm{x}})i_{\mathrm{dc}} + (L_{\mathrm{f}} + L_{\mathrm{dc}})\frac{\mathrm{d}i_{\mathrm{dc}}}{\mathrm{d}t} + E_{\mathrm{dc}}. \tag{17}$$

This equation can be applied in various contexts, such as deriving DC-side transfer functions for control purposes or determining the DC-side speed-torque characteristics of the PMSM, as demonstrated in the following section.

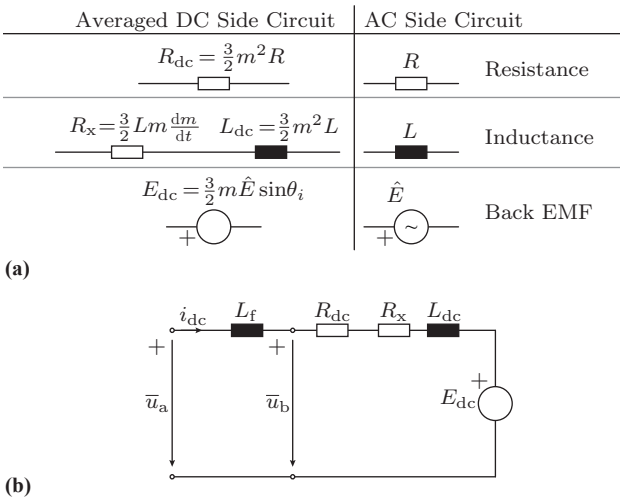

Fig. 3: **(a)** Summary of the expressions for the circuit components of the DC-side equivalent circuit of a CSI-supplied PMSM. **(b)** Complete DC-side circuit equivalent including the DC link inductor L_{f}.

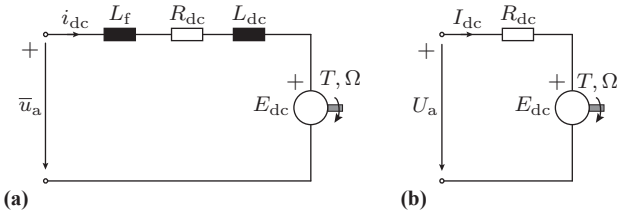

Fig. 4: **(a)** DC-side equivalent circuit of the CSI-supplied PMSM considering a constant modulation index $m = M$, therefore, $R_{\mathrm{x}} = 0$, see (14). **(b)** The DC-side speed-torque characteristic can be derived from the steady-state equivalent circuit, where inductances are not considered.

III. DC-Side Speed-Torque Characteristic

The primary goal of this paper is to simplify the control of the CSI-based drive system (depicted in **Fig. 1**) by decoupling the buck converter control from the CSI control. This is achieved by running the CSI in open loop, meaning its modulation index $m = M$ and current angle $\theta_i = \theta_I$ are fixed at constant values. Therefore, this results in $\frac{\mathrm{d}m}{\mathrm{d}t} = 0$ leading to $R_{\mathrm{x}} = 0$. Consequently, the circuit from **Fig. 3(b)** becomes like the one in **Fig. 4(a)**.

In this section, we aim to explore the mechanical aspects of the drive system by deriving the equivalent DC-side speed-torque characteristics of the open-loop controlled CSI supplying the PMSM.

Speed-torque characteristics are typically derived under steady-state operating conditions. Therefore, all quantities are assumed to be in a steady state. Since we have reduced the analysis to the DC side, steady-state conditions on the DC side imply that inductances can be neglected. Additionally, to clearly indicate the steady-state assumption, all quantities are represented using uppercase letters

$$\overline{u}_{\mathrm{a}} \to U_{\mathrm{a}} \quad \text{and} \quad i_{\mathrm{dc}} \to I_{\mathrm{dc}}, \tag{18}$$

and the same applies to the notation of the modulation index and the current angle

$$m \to M \quad \text{and} \quad \theta_i \to \theta_I. \tag{19}$$

The steady-state circuit used for this derivation is shown in **Fig. 4(b)**, leading to the following voltage balance equation:

$$U_\mathrm{a} = R_\mathrm{dc} I_\mathrm{dc} + E_\mathrm{dc}. \tag{20}$$

To derive the speed-torque characteristics, our objective is to relate the electrical quantities in (20) to the mechanical torque T and speed Ω of the PMSM. It should be noted that for electrical angular frequency, we use ω, and for the mechanical speed, we use Ω, and they are related via number of pole pairs p as

$$\omega = p\,\Omega. \tag{21}$$

Therefore, using (4), (16), and (21), we can relate E_dc to the mechanical speed Ω as

$$E_\mathrm{dc} = \frac{3}{2}\, M \sin\theta_I\, p\hat{\Psi} \cdot \Omega. \tag{22}$$

For PMSMs, a torque constant k_T relates the torque on the shaft T and the quadrature current $i_\mathrm{q} = \hat{I} \sin\theta_I$ as

$$T = k_\mathrm{T}\, \hat{I} \sin\theta_I. \tag{23}$$

It is known that this torque constant is determined by the PMSM's flux linkage $\hat{\Psi}$ and it is equal to

$$k_\mathrm{T} = \frac{3}{2}\, p\hat{\Psi}, \tag{24}$$

which allows us to rewrite (22) into the following form

$$E_\mathrm{dc} = M\, \sin\theta_I\, k_\mathrm{T}\, \Omega. \tag{25}$$

Using (23), we can relate torque of the PMSM T to the DC link current I_dc as

$$T = k_\mathrm{T}\, I_\mathrm{dc}\, M \sin\theta_I, \tag{26}$$

since $\hat{I} = M\, I_\mathrm{dc}$. Finally, using (9), (25), and (26), we can write the voltage balance equation (20) as a function of solely CSI and PMSM parameters as

$$U_\mathrm{a} = M^2\, \frac{3}{2} R\, \frac{T}{M \sin\theta_I\, k_\mathrm{T}} + M \sin\theta_I\, k_\mathrm{T}\, \Omega. \tag{27}$$

To get the DC-side speed-torque characteristic of the CSI-supplied PMSM, we need to rewrite (27) so that $\Omega = \Omega(U_\mathrm{a}, T)$, resulting in

$$\Omega = \frac{1}{M\, \sin\theta_I\, k_\mathrm{T}}\, U_\mathrm{a} - \frac{3}{2}\, \frac{R}{\sin^2\theta_I\, k_\mathrm{T}^2}\, T. \tag{28}$$

For the derived speed-torque characteristic (28), the no-load speed Ω_0 is obtained by assuming $T = 0$, which leads to

$$\Omega_0 = \frac{U_\mathrm{a}}{M\, \sin\theta_I k_\mathrm{T}}. \tag{29}$$

Similarly, the starting torque T_0 is obtained by solving (28) for T when $\Omega = 0$, resulting in

$$T_0 = \frac{2}{3}\, \frac{\sin\theta_I k_\mathrm{T}}{M\, R}\, U_\mathrm{a}. \tag{30}$$

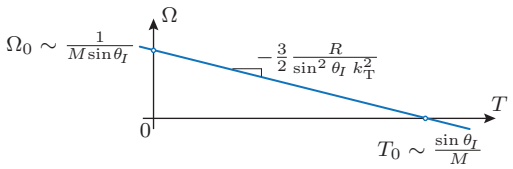

Fig. 5: DC-side speed-torque characteristic of the CSI-supplied PMSM. Reducing CSI's modulation index M expands the possible speed-torque area.

The derived speed-torque characteristic (28) is depicted in **Fig. 5**. It should be noted that, compared to the traditional DC machine speed-torque characteristic, the derived one can expand the speed-torque range by reducing the CSI's modulation index M. Also, the current angle θ_I that can be used for field-weakening of the PMSM in high-speed operation makes the characteristic steeper, leading to the speed being more sensitive to the load torques. For lower speeds, this angle is kept to $\theta_I = \frac{\pi}{2}$, resulting in $\sin\theta_I = 1$. Moreover, when comparing this to the traditional DC machine characteristics, $\sin\theta_I$ has the same effect on the characteristics as the excitation flux in a DC machine, while the CSI modulation index M plays a similar role to the number of turns on the rotor in a conventional DC machine.

IV. Equivalent DC Machine (E-DCM) Concept

As demonstrated in the analysis and derivations in **Sec. II** and **Sec. III**, the open-loop operated CSI, where the modulation index $m = M$ and the current angle $\theta_i = \theta_I$ are fixed, behaves from the DC side like a traditional DC machine, even though in reality it is a CSI supplying a PMSM. We refer to this concept as the *Equivalent DC Machine* (E-DCM) concept. The E-DCM concept offers significant advantages by simplifying the operation of the CSI drive system, allowing direct control of the torque on the PMSM shaft through the DC link current. Thus, the E-DCM concept provides users with the simplicity and familiarity of a DC machine, while in reality, a PMSM supplied by a CSI delivers higher torque and power density compared to a traditional DC machine, without the issues of commutation or maintenance, such as replacing brushes.

When using the E-DCM concept, the torque on the PMSM shaft is determined by equation (26), which shows that the torque is directly proportional to the DC link current. While this equation is derived for steady-state conditions, it remains valid for any dynamic situation, i.e., for any value of the DC link current i_dc. From equation (26), we can also derive the torque constant for the E-DCM concept, given by

$$k_\mathrm{Tdc} = k_\mathrm{T}\, M\, \sin\theta_I, \tag{31}$$

which represents the proportional relationship between the PMSM torque and the DC link current, i.e., $T = k_\mathrm{Tdc}\, i_\mathrm{dc}$. Since $0 \le M \le 1$ and $-1 \le \sin\theta_I \le 1$, the DC-side equivalent torque constant is maximized if $M = 1$ and

$\theta_I = \frac{\pi}{2}$, which leads to $k_{\mathrm{Tdc}} = k_{\mathrm{T}}$. Therefore, in further analysis, we will analyze E-DCM concept with

$$M = 1 \quad \text{and} \quad \theta_I = \frac{\pi}{2}, \tag{32}$$

as they maximize torque per DC link current ampere, ensuring the most efficient operation. Other parameter selections will be explored in future work.

When the E-DCM concept is employed in a CSI variable speed drive system, the conventional configuration shown in **Fig. 1** is transformed into the structure depicted in **Fig. 6**. In this setup, the input buck converter takes full control of the PMSM's speed and torque, just as it would in a conventional DC machine. Additionally, when the E-DCM concept is applied, as shown in **Fig. 6**, the CSI operates entirely in open loop, requiring no interaction from the user. This open-loop control for the CSI can be implemented on a microcontroller, or a dedicated IC can be designed to manage the CSI control, thereby eliminating any effort related to the CSI for the user of this drive system.

V. Simulation Results

To demonstrate the operation of the E-DCM concept in the CSI drive system, we implemented the configuration shown in **Fig. 6** in PLECS time-domain simulator, using the parameters outlined in **Tab. I**. Note that now speed control is performed directly with the input buck converter, where the PI speed controller C_Ω produces torque reference T^* that is, based on (26), used to obtain the DC link current reference $i^*_{\mathrm{dc}} = \frac{T^*}{k_{\mathrm{T}}}$. The PI current controller $\mathrm{C_i}$ provides the voltage reference that should be applied over the total DC resistance R_{dc} and inductance $L_{\mathrm{f}} + L_{\mathrm{dc}}$, see **Fig. 3(b)**. Analog to the DC machine armature current control, we help the current controller $\mathrm{C_i}$ by adding a feedforward value of the equivalent induced back EMF that can be obtained from mechanical speed Ω measurement as $E_{\mathrm{dc}} = k_{\mathrm{T}}\Omega$, see (25). Finally, the reference for the DC-link ('armature') voltage u^*_{a} is obtained and is used to calculate the duty cycle of the input buck converter and ultimately the gate signals of $\mathrm{T_H}$ and $\mathrm{T_L}$.

The time-domain simulation results are given in **Fig. 7**. The simulation waveforms show the acceleration of the PMSM from zero to nominal speed while being loaded with the torque linearly proportional to the speed $T = k_{\mathrm{fric}}\Omega$, where the friction coefficient is $k_{\mathrm{fric}} = 0.0507\,\mathrm{Nms}$, at which nominal mechanical power of $5\,\mathrm{kW}$ is developed for nominal mechanical speed of $3\,\mathrm{krpm}$. The mechanical speed Ω is shown in rpm in **Fig. 7(a)** and denoted as n_{mech}, which is calculated from Ω as

$$n_{\mathrm{mech}} = \Omega\,\frac{30}{\pi}. \tag{33}$$

It should be noted that the simulation starts from a standstill at which the DC link current and output capacitor voltages are zero. Therefore, the transient with currents in **Fig. 7(b)** shows a realistic response of the system, i.e., no initial values are set to help the simulation. It can be noticed that the DC link current quickly rises to its maximum value of $I_{\mathrm{dc,max}} = 30\,\mathrm{A}$ and makes PMSM produce the maximum torque that accelerates the drive system. Once the nominal speed is achieved, the DC link current drops down to the value of $10.8\,\mathrm{A}$ that produces the nominal torque on the machine at a nominal speed. Furthermore, the peak of AC currents of the PMSM $\hat{I}$ is equal to the DC link current i_{dc}, which is a property of the E-DCM concept due to the fixed modulation index $M = 1$. In **Fig. 7(c)**, the dq flux of the PMSM is depicted, which proves that by fixing the current angle to $\theta_I = \frac{\pi}{2}$, DC link current acts directly on the flux in q-axes, which proves that DC link current is purely torque producing current, i.e., quadrature current. The implemented modulation method for the CSI is based on the newly proposed algebraic modulation that does not use space vectors, see [15], resulting in the duty cycles for the high-side switches depicted in **Fig. 7(d)**.

Parameter	Symbol	Value
Buck		
Input voltage	U_{in}	$800\,\mathrm{V}$
Switching frequency	$f_{\mathrm{sw,b}}$	$80\,\mathrm{kHz}$
CSI		
DC link inductance	L_{f}	$450\,\mu\mathrm{H}$
Output capacitance	C_{f}	$0.1\,\mu\mathrm{F}$
Switching frequency	f_{sw}	$140\,\mathrm{kHz}$
Max. DC link current	$I_{\mathrm{dc,max}}$	$30\,\mathrm{A}$
PMSM		
Phase resistance	R	$0.2\,\Omega$
Phase inductance	L	$1\,\mathrm{mH}$
Number of pole pairs	p	5
Flux linkage	$\hat{\Psi}$	$0.2\,\mathrm{Wb}$
Moment of inertia	J	$0.001\,\mathrm{kgm}^2$
Nominal mech. power	P_{mech}	$5\,\mathrm{kW}$
Nominal mech. speed	n_{mech}	$3000\,\mathrm{rpm}$
Controller gains		
$\mathrm{C_i}$ closed-loop bandwidth	f_{cc}	$4\,\mathrm{kHz}$
$\mathrm{C_i}$ proportional gain	K_{pc}	$49\,\mathrm{V/A}$
$\mathrm{C_i}$ integral gain	K_{ic}	$10\,000\,\mathrm{V/(As)}$
C_Ω cross-over frequency	f_{cs}	$0.8\,\mathrm{kHz}$
C_Ω proportional gain	K_{ps}	$3.3\,\mathrm{sNm}$
C_Ω integral gain	K_{is}	$3400\,\mathrm{Nm}$

TABLE I: Simulation Parameters.

Tuning PI controllers for speed-controlled drive systems is well-established in the literature, see [16]. We start the controller design from the inner current controller by setting first a desired $\mathrm{C_i}$ closed-loop bandwidth of $f_{\mathrm{cc}} = 4\,\mathrm{kHz}$. By applying the pole-zero cancellation (PZC) method this results in analytic expressions for the PI gains: $K_{\mathrm{pc}} = \omega_{\mathrm{cc}}\,(L_{\mathrm{f}} + L_{\mathrm{dc}})$ and $K_{\mathrm{ic}} = \omega_{\mathrm{cc}}\,R_{\mathrm{dc}}$, where $\omega_{\mathrm{cc}} = 2\pi f_{\mathrm{cc}}$. Tuning the current controller in this way results in a closed-loop transfer function $\frac{\omega_{\mathrm{cc}}}{s+\omega_{\mathrm{cc}}}$ that is a first-order. The outer speed controller is tuned using the so-called symmetrical optimum, where the speed-cross-over frequency $f_{\mathrm{cs}} = 0.8\,\mathrm{kHz}$ is typically chosen to be five times lower than the current closed-loop bandwidth,

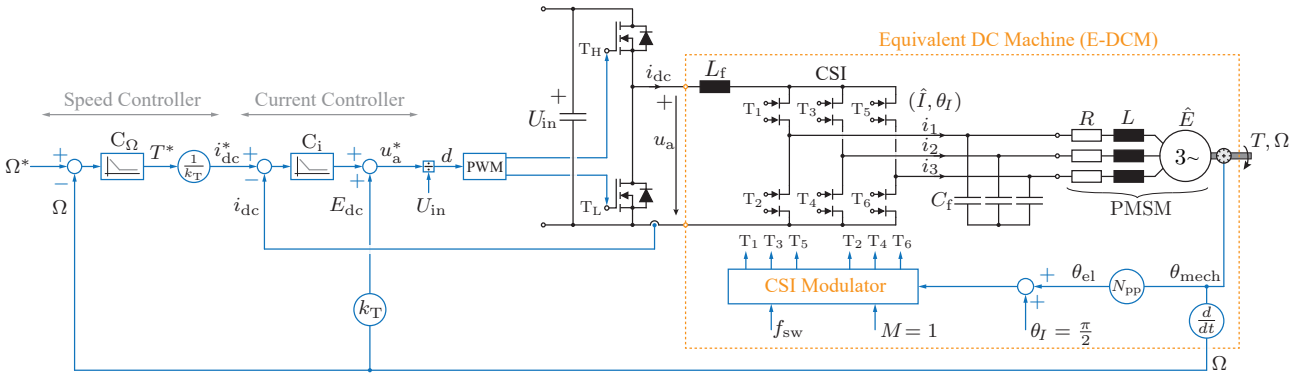

Fig. 6: Proposed speed control in the CSI-supplied drive system with PMSM is achieved using open-loop CSI control. This is implemented by fixing the modulation index at $M = 1$ and the current angle at $\theta_I = \pi/2$, and with the CSI relying solely on angle information from the encoder. This open-loop control of the CSI allows speed and torque control on the PMSM shaft to be fully managed by the input buck converter. Consequently, from the perspective of the input buck converter, the DC side of the CSI behaves exactly like a DC machine, which is why we refer to this control approach as the *Equivalent DC Machine* (E-DCM). For the selected values of M and θ_I, both the torque and voltage constants on the DC side are equivalent to the PMSM's torque constant k_T, as shown in equations (25) and (26).

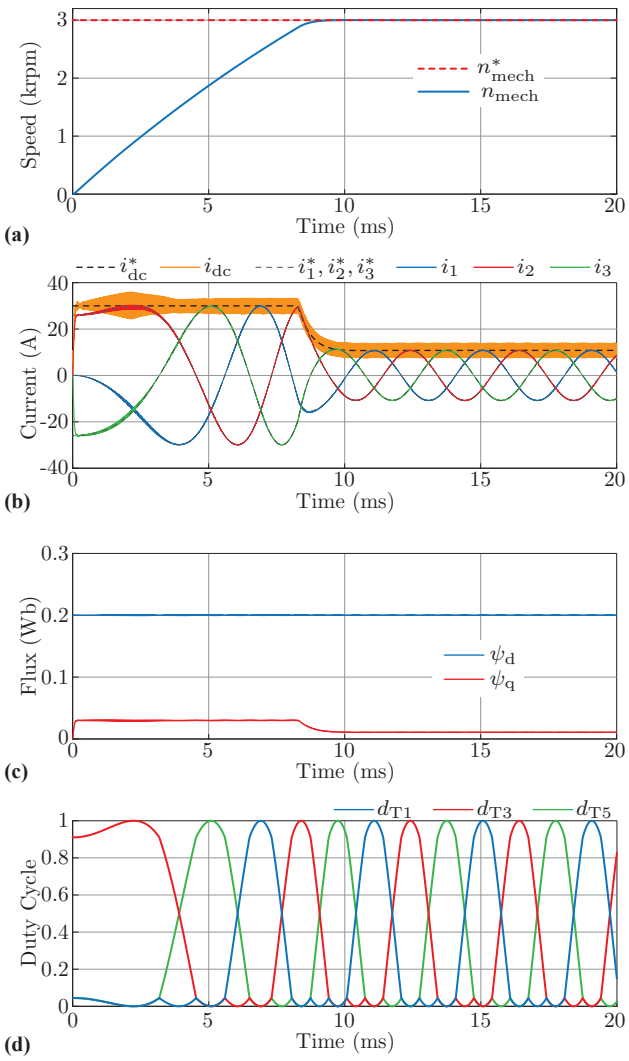

Fig. 7: Simulation waveforms for the CSI drive system from **Fig. 6**, verifying E-DCM concept: **(a)** mechanical speed, **(b)** DC-link and AC currents, **(c)** dq flux of the PMSM, and **(d)** duty cycles for the upper switches T_1, T_3, and T_5. The reference values are denoted with * and shown with dashed lines.

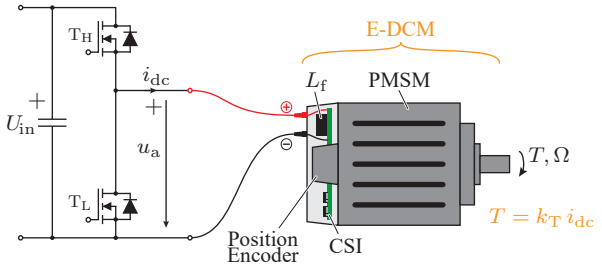

Fig. 8: Conceptual 2D prototype of a PMSM-integrated CSI. When the E-DCM concept is implemented, the system operates like a traditional DC machine, with the user simply connecting the positive and negative terminals. The CSI runs in an open loop, utilizing rotor shaft information from the integrated encoder.

i.e, $f_\mathrm{cs} = \frac{f_\mathrm{cc}}{5}$. The zero of the PI speed controller C_Ω needs to be five times lower than the speed cross-over frequency $f_\mathrm{pis} = \frac{f_\mathrm{cs}}{5}$ to ensure the open-loop transfer function pass through $0\,\mathrm{dB}$ with $-20\,\mathrm{dB/decade}$. This finally results in the analytic expressions for the speed-controller gains: $K_\mathrm{ps} = \frac{J\,\omega_\mathrm{cs}}{k_\mathrm{T}}$ and $K_\mathrm{is} = \omega_\mathrm{pis}\,K_\mathrm{ps}$, where $\omega_\mathrm{cs} = 2\pi f_\mathrm{cs}$ and $\omega_\mathrm{pis} = 2\pi f_\mathrm{pis}$. Finally, the gain values of both controllers are summarized in **Tab. I**.

A conceptual 2D prototype of the CSI-supplied PMSM that uses the proposed E-DCM control concept is illustrated in **Fig. 8**. This integrated drive consists of a DC link inductor L_f, a CSI, and a position encoder integrated into the casing of a PMSM, with the CSI operated as shown in **Fig. 6**. To run this motor-integrated drive system, the user simply connects the positive and negative terminals, as it functions like a DC machine, but in reality, CSI-supplied PMSM is operated.

VI. Conclusions

This paper focuses on a CSI drive system with an input buck stage that controls the DC link current, and a second CSI stage that supplies the PMSM. Conventionally, achieving speed control in such systems requires the

user to set a DC current reference and manage speed and torque control of the PMSM through field control using the CSI. In this paper, we propose a method to simplify such drive systems by operating the CSI in open loop, with a fixed modulation index. This approach allows the user to control the speed and torque of the PMSM directly through the input converter, where, under the open-loop operation of the CSI, the PMSM torque is directly proportional to the DC link current. This makes the CSI behave like a DC machine from the user's perspective, simplifying operation and control, and enabling broader and easier adoption of CSI drive systems in industry. We refer to this control concept as the *Equivalent DC Machine* (E-DCM) since the CSI supplying the PMSM behaves like a traditional DC machine on the DC side. Thus, the E-DCM concept combines the simplicity of a DC machine with the advantages of a PMSM, such as higher torque/power density and lower maintenance.

To validate this concept, we provided analytical derivations of the CSI's DC side equivalent circuit and developed the equivalent steady-state speed-torque characteristics. We then implemented a speed control for a $5\,\mathrm{kW}$ CSI-supplied PMSM, where the E-DCM concept was tested by accelerating the PMSM from zero to its nominal speed of $3000\,\mathrm{rpm}$. The results demonstrated a favorable speed transient response, with the PMSM's AC current peaks precisely tracking the DC link current, as expected for the E-DCM concept.

Our future work will focus on hardware verification of the E-DCM concept and extending its operating range to cover a wider range of speeds, which requires m and θ_i to be functions of mechanical speed Ω.

REFERENCES

[1] V. Madonna, G. Migliazza, P. Giangrande, E. Lorenzani, G. Buticchi, and M. Galea, "The rebirth of the current source inverter: Advantages for aerospace motor design," *IEEE Industrial Electronics Magazine*, vol. 13, no. 4, pp. 65–76, 2019.

[2] Y. Miyama, M. Hazeyama, S. Hanioka, N. Watanabe, A. Daikoku, and M. Inoue, "PWM carrier harmonic iron loss reduction technique of permanent-magnet motors for electric vehicles," *IEEE Transactions on Industry Applications*, vol. 52, no. 4, pp. 2865–2871, 2016.

[3] J. M. Erdman, R. J. Kerkman, D. W. Schlegel, and G. L. Skibinski, "Effect of PWM inverters on AC motor bearing currents and shaft voltages," *IEEE transactions on Industry Applications*, vol. 32, no. 2, pp. 250–259, 1996.

[4] G. L. Skibinski, R. J. Kerkman, and D. Schlegel, "EMI emissions of modern PWM AC drives," *IEEE Industry Applications Magazine*, vol. 5, no. 6, pp. 47–80, 1999.

[5] M. Kaufhold, H. Aninger, M. Berth, J. Speck, and M. Eberhardt, "Electrical stress and failure mechanism of the winding insulation in PWM-inverter-fed low-voltage induction motors," *IEEE Transactions on industrial electronics*, vol. 47, no. 2, pp. 396–402, 2000.

[6] M. Haider, M. Guacci, D. Bortis, J. W. Kolar, and Y. Ono, "Analysis and evaluation of active/hybrid/passive dv/dt-filter concepts for next generation SiC-based variable speed drive inverter systems," in *Proc. of IEEE Energy Conversion Congress and Exposition (ECCE-2020)*. IEEE, 2020, pp. 4923–4930.

[7] K. Shirabe, M. M. Swamy, J.-K. Kang, M. Hisatsune, Y. Wu, D. Kebort, and J. Honea, "Efficiency comparison between Si-IGBT-based drive and GaN-based drive," *IEEE Transactions on Industry Applications*, vol. 50, no. 1, pp. 566–572, 2013.

[8] F. Maislinger, H. Ertl, G. Stojcic, C. Lagler, and F. Holzner, "Design of a 100 khz wide bandgap inverter for motor applications with active damped sine wave filter," *The Journal of Engineering*, vol. 2019, no. 17, pp. 3766–3771, 2019.

[9] V. Madonna, P. Giangrande, W. Zhao, H. Zhang, C. Gerada, and M. Galea, "On the design of partial discharge-free low voltage electrical machines," in *Proc. of IEEE International Electric Machines & Drives Conference (IEMDC-2019)*. IEEE, 2019, pp. 1837–1842.

[10] M. Antivachis, D. Bortis, D. Menzi, and J. W. Kolar, "Comparative evaluation of Y-inverter against three-phase two-stage buck-boost DC-AC converter systems," in *Proc. of IEEE International Power Electronics Conference (IPEC-2018, ECCE Asia)*. IEEE, 2018, pp. 181–189.

[11] R. A. Torres, H. Dai, W. Lee, B. Sarlioglu, and T. Jahns, "Current-source inverter integrated motor drives using dual-gate four-quadrant wide-bandgap power switches," *IEEE Transactions on Industry Applications*, vol. 57, no. 5, pp. 5183–5198, 2021.

[12] J. Huber and J. W. Kolar, "Monolithic bidirectional power transistors," *IEEE Power Electronics Magazine*, vol. 10, no. 1, pp. 28–38, 2023.

[13] N. Nain, J. Huber, and J. W. Kolar, "Comparative evaluation of three-phase ac-ac voltage/current-source converter systems employing latest gan power transistor technology," in *Proc. of International Power Electronics Conference (IPEC-2022, ECCE Asia)*. IEEE, 2022, pp. 1726–1733.

[14] G. Migliazza, G. Buticchi, E. Carfagna, E. Lorenzani, V. Madonna, P. Giangrande, and M. Galea, "DC current control for a single-stage current source inverter in motor drive application," *IEEE Transactions on Power Electronics*, vol. 36, no. 3, pp. 3367–3376, 2020.

[15] P. Pejović, U. Borović, and S. Mirić, "Modulation in current source inverters: An algebraic approach," 2024, manuscript submitted for publication.

[16] S.-H. Kim, *Electric motor control: DC, AC, and BLDC motors*. Elsevier, 2017.